Numerical study of Bragg CDI on thick polycrystalline specimens

Pedersen, Anders Filsøe; Chamard, Virginie; Poulsen, Henning Friis

Published in:
Optics Express

Link to article, DOI:
10.1364/OE.26.023411

Publication date:
2018

Document Version
Publisher's PDF, also known as Version of record

Research Article | Vol. 26, No. 18 | 3 Sep 2018 | OPTICS EXPRESS 23411
Optics EXPRESS

Numerical study of Bragg CDI on thick polycrystalline specimens

ANDERS FILSØE PEDERSEN,[1] VIRGINIE CHAMARD,[2] AND HENNING FRIIS POULSEN[1,*]

[1]*Department of Physics, Technical University of Denmark, Fysikvej 307, 2800 Kongens Lyngby, Denmark*
[2]*Aix Marseille Univ, CNRS, Centrale Marseille, Institut Fresnel, Marseille, France*
**hfpo@fysik.dtu.dk*

Abstract: Bragg coherent diffraction imaging (BCDI) is a powerful X-ray imaging technique for crystalline materials, providing high resolution maps of structure and strain. The technique is typically used to study a small isolated object, and is in general not compatible with a bulk polycrystalline sample, due to overlap of diffraction signals from various crystalline elements. In this paper, we present an imaging method for bulk samples, based on the use of a coherent source. The diffracted X-ray beam from a grain or domain of choice is magnified by an objective before being monitored by a 2D detector in the far field. The reconstruction principle is similar to the case of BCDI, while taking the magnification and pupil function into account. The concept is demonstrated using numerical simulations and reconstructions. We find that by using an object-lens distance shorter than the focal length, the numerical aperture is larger than in a traditional imaging geometry, and at the same time the setup is insensitive to small phase errors by lens imperfections. According to our simulations, we expect to be able to achieve a spatial resolution smaller than 20 nm when using the objective lens in this configuration.

OCIS codes: (110.1650) Coherence imaging; (110.7440) X-ray imaging.

References

1. J. Miao, P. Charalambous, J. Kirz, and D. Sayre, "Extending the methodology of X-ray crystallography to allow imaging of micrometre-sized non-crystalline specimens," Nature **400**(6742), 342–344 (1999).
2. J. Miao, T. Ishikawa, I. K. Robinson, and M. M. Murnane, "Beyond crystallography: diffractive imaging using coherent x-ray light sources," Science **348**(6234), 530–535 (2015).
3. S. Marchesini, "Invited article: a [corrected] unified evaluation of iterative projection algorithms for phase retrieval," Rev. Sci. Instrum. **78**(1), 011301 (2007).
4. D. Sayre, "Some implications of a theorem due to Shannon," Acta Crystallogr. **5**(6), 843 (1952).
5. R. Harder and I. K. Robinson, "Coherent X-Ray Diffraction Imaging of Morphology and Strain in Nanomaterials," JOM **65**(9), 1202–1207 (2013).
6. A. Yau, W. Cha, M. W. Kanan, G. B. Stephenson, and A. Ulvestad, "Bragg coherent diffractive imaging of single-grain defect dynamics in polycrystalline films," Science **356**(6339), 739–742 (2017).
7. J. N. Clark, L. Beitra, G. Xiong, A. Higginbotham, D. M. Fritz, H. T. Lemke, D. Zhu, M. Chollet, G. J. Williams, M. Messerschmidt, B. Abbey, R. J. Harder, A. M. Korsunsky, J. S. Wark, and I. K. Robinson, "Ultrafast Three-Dimensional Imaging of Lattice Dynamics in Individual Gold Nanocrystals," Science **341**(6141), 56–59 (2013).
8. M. A. Pfeifer, G. J. Williams, I. A. Vartanyants, R. Harder, and I. K. Robinson, "Three-dimensional mapping of a deformation field inside a nanocrystal," Nature **442**(7098), 63–66 (2006).
9. S. Takagi, "A Dynamical Theory of Diffraction for a Distorted Crystal," J. Phys. Soc. Jpn. **26**(5), 1239–1253 (1969).
10. A. I. Pateras, M. Allain, P. Godard, L. Largeau, G. Patriarche, A. Talneau, K. Pantzas, M. Burghammer, A. A. Minkevich, and V. Chamard, "Nondestructive three-dimensional imaging of crystal strain and rotations in an extended bonded semiconductor heterostructure," Phys. Rev. B **92**(20), 205305 (2015).
11. V. Chamard, M. Allain, P. Godard, A. Talneau, G. Patriarche, and M. Burghammer, "Strain in a silicon-on-insulator nanostructure revealed by 3D x-ray Bragg ptychography," Sci. Rep. **5**(1), 9827 (2015).
12. S. J. Leake, M. C. Newton, R. Harder, and I. K. Robinson, "Longitudinal coherence function in X-ray imaging of crystals," Opt. Express **17**(18), 15853–15859 (2009).
13. P. Godard, M. Allain, and V. Chamard, "Imaging of highly inhomogeneous strain field in nanocrystals using x-ray Bragg ptychography: A numerical study," Phys. Rev. B **84**(14), 144109 (2011).

#328815 https://doi.org/10.1364/OE.26.023411
Journal © 2018 Received 9 May 2018; revised 4 Aug 2018; accepted 16 Aug 2018; published 28 Aug 2018

Optics EXPRESS

14. A. A. Minkevich, M. Gailhanou, J.-S. Micha, B. Charlet, V. Chamard, and O. Thomas, "Inversion of the diffraction pattern from an inhomogeneously strained crystal using an iterative algorithm," Phys. Rev. B **76**(10), 104106 (2007).
15. F. Mastropietro, P. Godard, M. Burghammer, C. Chevallard, J. Daillant, J. Duboisset, M. Allain, P. Guenoun, J. Nouet, and V. Chamard, "Revealing crystalline domains in a mollusc shell single-crystalline prism," Nat. Mater. **16**(9), 946–952 (2017).
16. H. F. Poulsen, *Three-Dimensional X-Ray Diffraction Microscopy* (Springer, 2004).
17. H. F. Poulsen, "An introduction to three-dimensional X-ray diffraction microscopy," J. Appl. Cryst. **45**(6), 1084–1097 (2012).
18. W. Ludwig, S. Schmidt, E. M. Lauridsen, and H. F. Poulsen, "X-ray diffraction contrast tomography: a novel technique for three-dimensional grain mapping of polycrystals. I. Direct beam case," J. Appl. Cryst. **41**(2), 302–309 (2008).
19. H. Simons, A. King, W. Ludwig, C. Detlefs, W. Pantleon, S. Schmidt, I. Snigireva, A. Snigirev, H. F. Poulsen, and H. F. Poulsen, "Dark-field X-ray microscopy for multiscale structural characterization," Nat. Commun. **6**(1), 6098 (2015).
20. H. Simons, S. R. Ahl, H. F. Poulsen, and C. Detlefs, "Simulating and optimizing compound refractive lens-based X-ray microscopes," J. Synchrotron Radiat. **24**(2), 392–401 (2017).
21. H. Simons, A. C. Jakobsen, S. R. Ahl, C. Detlefs, and H. F. Poulsen, "Multiscale 3D characterization with dark-field x-ray microscopy," MRS Bull. **41**(06), 454–459 (2016).
22. A. F. Pedersen, H. Simons, C. Detlefs, and H. F. Poulsen, "The fractional Fourier transform as a simulation tool for lens-based X-ray microscopy," J. Synchrotron Radiat. **25**(3), 717–728 (2018).
23. A. F. Pedersen, *Andersfp/XFrFT: XFrFT* (Zenodo, 2017).
24. F. Seiboth, A. Schropp, M. Scholz, F. Wittwer, C. Rödel, M. Wünsche, T. Ullsperger, S. Nolte, J. Rahomäki, K. Parfeniukas, S. Giakoumidis, U. Vogt, U. Wagner, C. Rau, U. Boesenberg, J. Garrevoet, G. Falkenberg, E. C. Galtier, H. Ja Lee, B. Nagler, and C. G. Schroer, "Perfect X-ray focusing via fitting corrective glasses to aberrated optics," Nat. Commun. **8**, 14623 (2017).
25. L. W. Whitehead, G. J. Williams, H. M. Quiney, D. J. Vine, R. A. Dilanian, S. Flewett, K. A. Nugent, A. G. Peele, E. Balaur, and I. McNulty, "Diffractive Imaging Using Partially Coherent X Rays," Phys. Rev. Lett. **103**(24), 243902 (2009).
26. J. N. Clark, X. Huang, R. Harder, and I. K. Robinson, "High-resolution three-dimensional partially coherent diffraction imaging," Nat. Commun. **3**(1), 993 (2012).
27. W. Cha, S. Song, N. C. Jeong, R. Harder, K. B. Yoon, I. K. Robinson, and H. Kim, "Exploration of crystal strains using coherent x-ray diffraction," New J. Phys. **12**(3), 035022 (2010).
28. J. R. Fienup, "Phase retrieval algorithms: a comparison," Appl. Opt. **21**(15), 2758–2769 (1982).
29. S. Marchesini, H. He, H. N. Chapman, S. P. Hau-Riege, A. Noy, M. R. Howells, U. Weierstall, and J. C. H. Spence, "X-ray image reconstruction from a diffraction pattern alone," Phys. Rev. B **68**(14), 140101 (2003).
30. D. Shapiro, P. Thibault, T. Beetz, V. Elser, M. Howells, C. Jacobsen, J. Kirz, E. Lima, H. Miao, A. M. Neiman, and D. Sayre, "Biological imaging by soft x-ray diffraction microscopy," Proc. Natl. Acad. Sci. U.S.A. **102**(43), 15343–15346 (2005).
31. R. Harder, M. A. Pfeifer, G. J. Williams, I. A. Vartaniants, and I. K. Robinson, "Orientation variation of surface strain," Phys. Rev. B **76**(11), 115425 (2007).
32. H. F. Poulsen, A. C. Jakobsen, H. Simons, S. R. Ahl, P. K. Cook, and C. Detlefs, "X-ray diffraction microscopy based on refractive optics," J. Appl. Cryst. **50**(5), 1441–1456 (2017).
33. T. Roth, C. Detlefs, I. Snigireva, and A. Snigirev, "X-ray diffraction microscopy based on refractive optics," Opt. Commun. **340**, 33–38 (2015).
34. J. Hilhorst, F. Marschall, T. N. Tran Thi, A. Last, and T. U. Schülli, "Full-field X-ray diffraction microscopy using polymeric compound refractive lenses," J. Appl. Cryst. **47**(6), 1882–1888 (2014).
35. A. J. Morgan, M. Prasciolu, A. Andrejczuk, J. Krzywinski, A. Meents, D. Pennicard, H. Graafsma, A. Barty, R. J. Bean, M. Barthelmess, D. Oberthuer, O. Yefanov, A. Aquila, H. N. Chapman, and S. Bajt, "High numerical aperture multilayer Laue lenses," Sci. Rep. **5**(1), 9892 (2015).
36. M. Prasciolu, A. F. G. Leontowich, J. Krzywinski, A. Andrejczuk, H. N. Chapman, and S. Bajt, "Fabrication of wedged multilayer Laue lenses," Opt. Mater. Express **5**(4), 748–755 (2015).
37. A. Andrejczuk, J. Krzywinski, and S. Bajt, "Influence of imperfections in a wedged multilayer Laue lens for the focusing of X-rays investigated by beam propagation method," Nucl. Instrum. Methods Phys. Res. Sect. B Beam Interact. Mater. At. **364**, 60–64 (2015).
38. P. Godard, G. Carbone, M. Allain, F. Mastropietro, G. Chen, L. Capello, A. Diaz, T. H. Metzger, J. Stangl, and V. Chamard, "Three-dimensional high-resolution quantitative microscopy of extended crystals," Nat. Commun. **2**(1), 568 (2011).
39. S. O. Hruszkewycz, M. Allain, M. V. Holt, C. E. Murray, J. R. Holt, P. H. Fuoss, and V. Chamard, "High-resolution three-dimensional structural microscopy by single-angle Bragg ptychography," Nat. Mater. **16**(2), 244–251 (2017).

Optics EXPRESS

1. Introduction

Coherent X-ray diffraction imaging, CDI, is a microscopy method aiming at producing a highly resolved quantitative image of a sample illuminated by a coherent plane wave without the need of an objective [1,2]. It relies on the inversion of a 3D set of intensity patterns to retrieve the phase of the scattered wave-fields [3]. To solve the phase problem, iterative algorithms have been developed, based on the so-called support condition, which imposes the object to be contained in a finite volume, so that the corresponding diffraction pattern is oversampled by at least twice the Nyquist frequency in all 3 dimensions [4]. Hence, instead of performing imaging by means of lenses, numerical approaches are used to produce a 3D image of the electron density of the object, at spatial resolutions ultimately limited by the inverse of the probed wave-vector transfer maximum [5].

CDI approaches are particularly relevant for crystalline imaging, as recently illustrated by the *in-operando* monitoring of the motion of a dislocation [6] and the propagation of a shockwave [7]. Those specific crystalline imaging methods, referred to as Bragg coherent diffraction imaging (BCDI), exploit the oversampled intensity patterns measured in the vicinity of a Bragg peak produced by a finite-sized crystal under hard X-ray illumination [8]. In this configuration, the full 3D intensity pattern is derived from 2D patterns acquired at equidistant angular positions during a scan where the sample is tilted around an axis perpendicular to the incoming beam. Typically, this “rocking-scan” extends over a limited angular range of about 0.1-1°. The retrieved 3D effective electron density map contains information on both electron density distribution and crystalline displacements within the sample [9]. From the crystalline displacement information, one can derive 3D strain and rotation maps of the probed crystalline plane family [10]. Spatial resolutions in the 10 nm range can be obtained with strain sensitivity in the order of a few times 10^{-4} [11]. The performance is even expected to improve with the introduction of diffraction limited synchrotron sources.

In spite of its recent achievements, the current use of BCDI is limited to address solely a specific class of crystalline materials: (sub-)micrometer sized isolated crystals exhibiting rather homogeneous strain fields. This limitation arises from the need of a finite support constraint. Indeed, this constraint requires the diffraction volume to satisfy the coherence requirements [12] of the experimental set-up as defined by the beam and detection frame properties. The limitation on strain is a side effect of this support condition: for crystals with large strain gradients the far-field propagation of the support function does not correlate with the distribution of the highly distorted scattered field, particularly for photon limited diffraction patterns [13]. Hence, the support condition does not bring useful information to the phase problem, which can be solved only if additional *a priori* knowledge is available [14]. Bragg ptychography has been proposed to address the case of an extended crystal, but it still requires that the sample fulfills the longitudinal coherence length condition (implying a limit on thickness of typically about 1 μm) [15]. However, many areas of research encountered in materials science, engineering, and geoscience, require the investigations of thicker samples comprised of a myriad of micro-crystals producing super-imposed diffraction Bragg peaks. For such samples, none of the above approaches are applicable, because simultaneously diffracting micro-crystals would be contained in a volume much larger than the coherence volume, while the superposition of their individual diffraction patterns, potentially corresponding to different strain levels may resemble the behavior of a single highly strained crystal.

For 3D mapping of mm-sized polycrystalline materials X-ray imaging methods based on diffraction tomography approaches are in use: 3D X-ray diffraction (3DXRD) [16,17] and diffraction contrast tomography (DCT) [18]. Space-filling 3D maps of orientations and strain tensors can be obtained for thousands of grains, however with a spatial resolution of at best 2 microns. Inserting a lens as an objective in the diffracted beam from one such grain, one may generate a magnified 3D grain map with currently 100 nm resolution [19]. In theory the latter method, known as dark field X-ray microscopy (DFXRM), is compatible with a much-improved spatial resolution. In practice, it is limited in two ways. Firstly, by manufacturing

Optics EXPRESS

errors of the lenses available leading to aberrations (thicker samples require higher X-ray energies, which points to compound refractive lenses, CRLs, as the optics of choice). Secondly, DFXRM (as well as 3DXRD and DCT) is based on kinematical diffraction theory requiring the measurement volume to be larger than the coherence volume.

In this work, we propose a new implementation of BCDI, which is able to overcome the finite-size problem and provide highly resolved 3D images of single interior crystals within a thick poly-crystalline sample. The experimental set-up is a generalization of the classical BCDI configuration, where - similar to DFXRM - we place an X-ray lens in the diffracted beam from one selected interior crystal (which depending on context may be a grain or a domain). The small angular acceptance of the lens behaves as a spatial filter [19,20], which drastically reduces the diffracting volume. The 3D coherent diffraction pattern of the chosen crystal therefore is not superposed upon the diffraction pattern of other crystals. Hence, it can be extracted and further inverted. However, the introduction of a lens, which modifies the scattered wave-field, may deteriorate the image quality. Based on numerical simulations, we show in this paper that our novel approach – objective BCDI - can be compatible with high-quality images. We expect our approach to be relevant in the framework of multi-scale microscopy, e.g. in combination with 3DXRD and DFXRM [21]. Such an instrument is planned at the European Synchrotron Radiation Facility, ESRF. The target crystal size would be the same as for classical BCDI, of order 1 µm, while the sample-to-objective distance would be similar to DFXRM work, of order 5-30 cm. For most materials absorption would appear simply as a constant normalization factor on all intensities.

The article is organized as follow: the first section presents the strategy underlying the introduction of a lens behind the sample. The second section details the chosen numerical model including the sample and the propagation of the diffracted field downstream to the detection plane. Simulations are performed for two configurations: classical lensless BCDI and our objective BCDI approach. These simulations will be used in the third section to quantify the performance of objective BCDI with respect to classical BCDI, together with a detailed interpretation of the obtained results. Finally, a last section comprises a discussion of the limitations and further opportunities for this technique.

2. Objective based Bragg coherent diffraction imaging

BCDI requires that the diffraction volume fulfills the coherence length conditions [12] and that the information encoded in the diffraction pattern can directly be linked to the overall shape of the diffracting volume [13]. These conditions are not met when a finite-sized beam illuminates a polycrystalline material: for a fixed angular position of the detection, corresponding to the Bragg angle of a chosen Bragg reflection, several crystalline parts along the incoming beam path will simultaneously fulfill the diffraction conditions. Hence crystalline regions, located at distances corresponding to beam path differences larger than the longitudinal coherence length, will individually produce a diffraction pattern, which will incoherently overlap with each other in the detection plane. Moreover, in the more optimal case where all the diffracting parts are contained within the coherence volume, the coherent superposition of all the respective wave-fields is expected to produce a highly distorted diffraction pattern, for which the support condition will likely fail in constraining the reconstruction process. Therefore, in order to study bulk polycrystalline specimens a drastic reduction of the diffracting volume is required. This can be achieved by introducing a finite aperture element behind the sample, so that the diffracting volume corresponds to the intersection of the incoming beam and exit beam transmitted by the finite aperture element, as illustrated in Fig. 1(a). One notes that the larger the diffraction angle 2θ, the more efficient the spatial filter becomes. If a thick objective such as a CRL replaces the finite size aperture, the situation becomes even more favorable because the stack of lenses acts as a collimation path.

Optics EXPRESS

Contrary to the classical BCDI configuration (Fig. 1(b)), the objective implies the existence of an image plane and consequently a magnified image. To introduce the geometry let us first assume the objective to behave as a thin lens. In this case the following equations apply:

$$\frac{1}{d_1}+\frac{1}{d_2}=\frac{1}{f}, \tag{1a}$$

$$M=-\frac{d_2}{d_1}, \tag{1b}$$

$$NA=\frac{D}{d_1}, \tag{1c}$$

where d_1 is the sample-objective distance, d_2 is the objective-image plane distance, f is the focal distance of the objective, M is the magnification, and NA is the numerical aperture as defined by the effective aperture of the lens, D. In Fig. 1(c) we show a simple realization of the lens set-up with $M = -1$, a real image. The wavefield in the image plane is then an inverted version of the exit field from the sample – as seen in the angular direction of the lens and detector. The full 3D components of the exit field can be acquired with the usual tomographic approach.

By virtue of the diffraction theorem, the numerical aperture limits the spatial resolution that can be provided by means of BCDI algorithms based on the observed coherent diffraction pattern at the far field detector. Notably, in comparison to classical CDI there are two additional degrees of freedom in the set-up, parameterized by e.g. M and d_1. Varying these impacts the spatial resolution, the efficiency of data acquisition, and the distance from sample to the first optical element. Depending on the parameters, one may operate with a real image (if $d_1 > f$) or a virtual image (if $d_1 < f$). As an example in Fig. 1(d), we sketch a set-up with a virtual image of the exit field with a magnification of $M = 1.5$, propagating downstream to the detection plane. In this configuration, the numerical aperture, and therefore spatial resolution, is improved with respect to the configuration in Fig. 1(c), at the expense of increasing the image-detector distance in order to preserve the sampling ratio with respect to the no-lens case (Fig. 1(b)).

In reality the thin lens approximation is not valid for a CRL. Based on geometrical optics accurate closed form expressions for a CRL with N identical lenslets placed a distance T apart have been established [20]. Equations (1) are replaced by:

$$f_N = f\varphi\cot\left(N\varphi\right),\varphi=\sqrt{T/f},\# \tag{2a}$$

$$\frac{1}{d_1}+\frac{1}{d_2}-\frac{1}{f_N}+\frac{f\varphi\tan\left(N\varphi\right)}{d_1 d_2}=0,\# \tag{2b}$$

$$M=-\frac{d_2\sin\left(N\varphi\right)}{f\varphi}+\cos\left(N\varphi\right),\# \tag{2c}$$

$$NA=2.35\sigma_a,\# \tag{2d}$$

where f is the focal length of each lenslet, φ is related to the focusing power per length, f_N is the effective focal length of the whole CRL, and σ_a is the RMS width of the Gaussian angular acceptance function (see [20]).

Optics EXPRESS

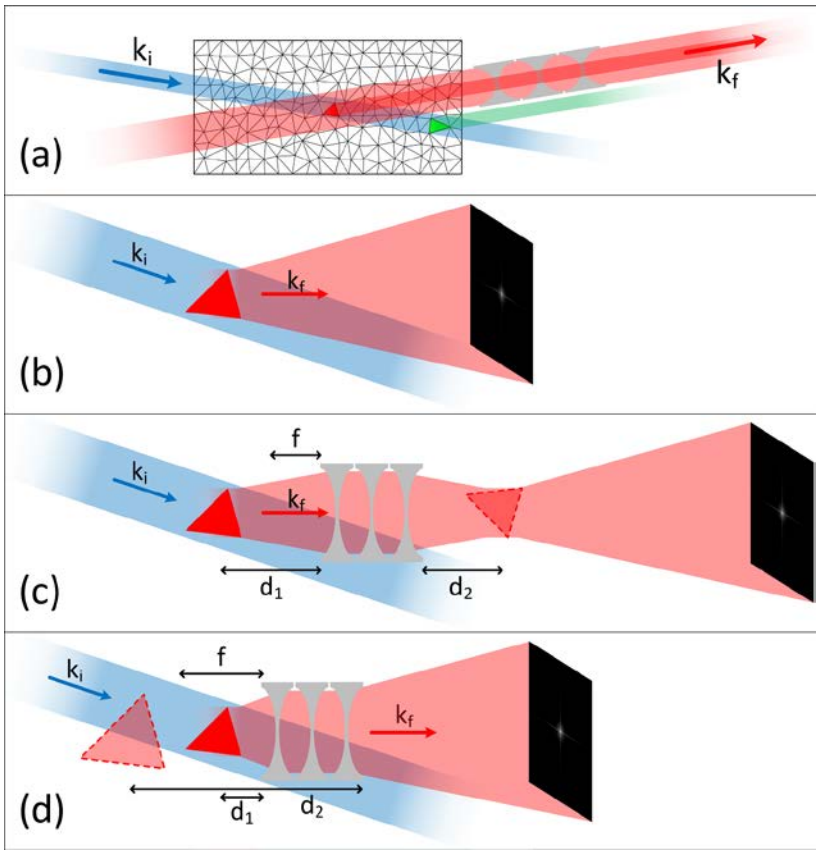

Fig. 1. BCDI with an objective lens for imaging poly-crystalline material: (a) Selection of the diffracting crystal with a finite size optical element placed on the detection arm. (b) The classical BCDI configuration. (c) Objective BCDI introducing a lens in a 1:1 configuration and (d) Objective BCDI with a lens using a 1:2 virtual image. The components are not to scale, but the relative image-detector distances are correct.

3. The numerical model – sample design and scattered wave propagation

The proposed concept has been tested by comparing numerical simulations for the objective configuration with that of classical BCDI. The simulations consider the full 3D case of BCDI and assume a fully coherent incoming beam.

Optics EXPRESS

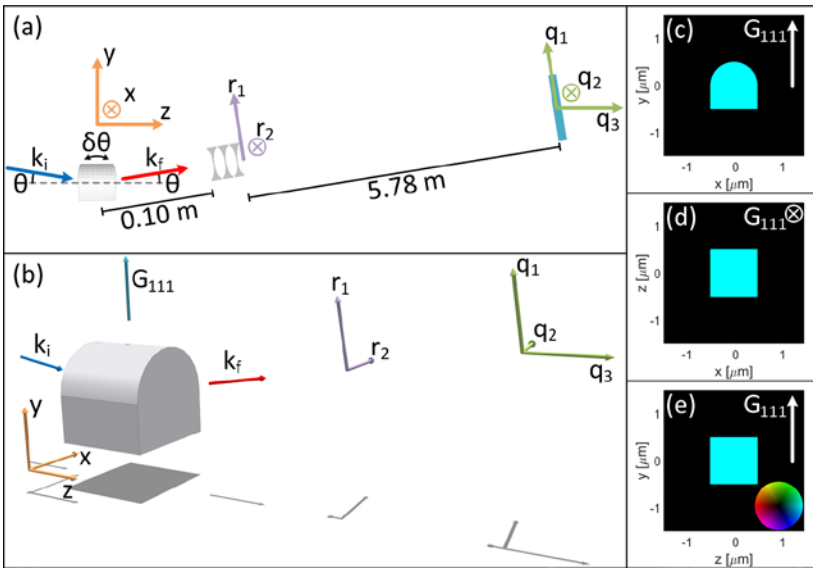

Fig. 2. The numerical model. (a) The 3D BCDI geometry with the object coordinate system (**x**, **y**, **z**), and the incident ($\mathbf{k}_i$) and exit ($\mathbf{k}_f$) angles are θ. During a rocking scan the object is rotated by δθ around the x-axis. The CRL objective lens is placed along the axis of the exit beam, and the real space coordinate at its exit plane is ($\mathbf{r}_1$, $\mathbf{r}_2$). The detector is used to record the reciprocal space ($\mathbf{q}_1$, $\mathbf{q}_2$, $\mathbf{q}_3$). (b) 3D rendering of the test micro-crystal, a cube with a cylindrical top. The $\mathbf{k}_i$, $\mathbf{k}_f$ and chosen Bragg vector $(\mathbf{G})_{111}$ are indicated along with the other coordinate axes in (a). (c)-(e) Cross sections of the test object along the laboratory frame planes, the (**x**, **y**), (**z**, **y**) and (**x**, **z**) planes, respectively. The brightness indicates the density and the color indicate the phase, following the color scale provided as an inset of (e).

3.1 Experimental

The 3D Bragg diffraction geometry is depicted in Fig. 2(a). The sample is illuminated by a planar wavefront described by its wave-vector $\mathbf{k}_i$, while the intensity is measured in a 2D detection plane, in which each pixel is characterized by an exit wave-vector $\mathbf{k}_f$ (with $k_{i,f} = 2\pi/\lambda$, where λ is the wavelength of the X-ray beam). In the Bragg condition for a given *hkl* Bragg reflection with vector $\mathbf{G}_{hkl}$, the angle between $\mathbf{k}_i$ and the central $\mathbf{k}_f$ is $2\theta_B$, with θ_B symbolizing the Bragg angle of the chosen reflection. In order to access the 3D components of the intensity, the sample is angularly scanned along the rocking curve, i.e. the incident and exit angles are simultaneously changed by an opposite angular amount in steps of δθ. At each angular position a 2D intensity pattern is recorded, corresponding to a 2D plane within the reciprocal space, each shifted incrementally in the direction perpendicular to the $\mathbf{G}_{hkl}$ Bragg vector. Thereby, the 3D intensity distribution is obtained by stacking the successive 2D intensity patterns. The intensity is recorded as a function of the wave-vector transfer $\mathbf{q} = \mathbf{k}_f - \mathbf{k}_i - \mathbf{G}_{hkl}$ (note that for sake of simplicity, $\mathbf{q} = 0$ when the Bragg condition is exactly met). Hence, a natural 3D detection frame is the ($\mathbf{q}_1$, $\mathbf{q}_2$, $\mathbf{q}_3$) reciprocal space frame where $\mathbf{q}_1$ and $\mathbf{q}_2$ are along the 2 principal directions of the detection plane (with $\mathbf{q}_1$ in the diffraction plane, making an angle θ_B to $\mathbf{G}_{hkl}$, and $\mathbf{q}_2$ perpendicular to the diffraction plane), while $\mathbf{q}_3$ is along the rocking curve scanning direction, i.e. perpendicular to $\mathbf{G}_{hkl}$. Note that this natural coordinate system is not orthogonal, however easy to transform into an orthogonal frame if necessary [8]. In the real space, the sample is described in the laboratory frame (**x**, **y**, **z**) with **y** being parallel to $\mathbf{G}_{hkl}$, **x** being perpendicular to $\mathbf{G}_{hkl}$ and $\mathbf{k}_i$ (and $\mathbf{k}_f$), and **z** being perpendicular to **x** and **y** so that (**x**, **y**, **z**) is a right-handed orthonormal frame (see Figs. 2(a) and 2(b)). For the objective BCDI configuration, a lens is positioned behind the sample, with its exit plane parallel to the detection plane. Therefore, two additional direct space axes are introduced, $\mathbf{r}_1$ and $\mathbf{r}_2$, parallel to $\mathbf{q}_1$ and $\mathbf{q}_2$, respectively (see Figs. 2(a) and 2(b)).

Optics EXPRESS

3.2 Sample model

The simulations are based on a sample with a simple geometry, as shown in Fig. 2(b). The sample is a 1 μm^3 cube, in which the central symmetry has been broken by the introduction of a cylindrical surface at its top (see Visualization 1 for a 3D rendering). Its cross sections are illustrated in Figs. 2(c)-2(e). In BCDI, the scattering function of a crystalline sample is described by an effective electron density $\rho(\mathbf{r}) = |\rho(\mathbf{r})|\exp(i\phi(\mathbf{r}))$, where the amplitude $|\rho(\mathbf{r})|$ describes the average electron density distribution and the phase $\phi(\mathbf{r})$ corresponds to the projection of the crystalline displacement field $\mathbf{u}(\mathbf{r})$ onto the Bragg vector, so that $\phi(\mathbf{r}) = \mathbf{u}(\mathbf{r})\cdot\mathbf{G}_{hkl}$. In this work, for simplicity, the density of the crystal is set to be homogenous (and equal to 1) while its phase has been fixed to 0, indicating that the crystal is homogenously strained with respect to a reference strain state, which is the crystal lattice itself. In a real sample, the phase is expected to be more complex. However, this simple phase field will allow us to quantify the quality of the retrieved image, while avoiding non-convergence issues often encountered during the retrieval of non-homogenously strained crystals in BCDI.

3.3 Forward propagation approach

For calculating the scattered intensities in the detection plane, the fractional Fourier transform (FrFT) approach to wavefield propagation is used for both configurations. The principles of the FrFT propagation is described in [22]: it has no sampling requirements, it is fast and well suited for propagation along a finite distance or through CRLs. (Note that the XFrFT simulation package is available at [23]). Given the wave-field in any plane, it enables calculating the 2D wave-field propagated (or back-propagated) to any other plane. In this work, the initial wave-fields are the series of the 2D exit fields at the sample position obtained along the rocking curve. These are obtained as follows: the 3D sample scattering function is transferred into the space conjugated to the ($\mathbf{q}_1$, $\mathbf{q}_2$, $\mathbf{q}_3$) detection frame before applying a 3D fast Fourier transform (FFT), in order to obtain a 3D far-field wave-field diffraction pattern $E(\mathbf{q})$. According to the Fourier slice theorem, each $E(\mathbf{q})$ described in the ($\mathbf{q}_1$, $\mathbf{q}_2$) planes and taken along the $\mathbf{q}_3$ direction can be associated (by a 2D inverse FFT, IFFT, operation) with the projection of the object scattering function, projected along the $\mathbf{q}_3$ direction: these are nothing else but the series of 2D sample exit fields, $\psi_i(\mathbf{r})$, produced along the rocking curve scan. This numerical approach is summarized in Fig. 3(a).

Using the set of 2D sample exit fields, $\psi_i(\mathbf{r})$, the 3D intensity patterns are produced for the BCDI and objective BCDI configurations. For the first one, each 2D sample exit field is propagated by the sample-detector distance to the detection plane. The 2D intensity patterns, $I(\mathbf{q})$, are calculated by $I(\mathbf{q}) = |E(\mathbf{q})|^2$ and the 3D intensity matrix is obtained by stacking these 2D intensity patterns. For the objective BCDI case, the 2D field propagation is carried out in 4 steps. First, the exit field, $\psi_i(\mathbf{r})$, is multiplied by the vignetting function in the sample plane (limiting the field of view) [20,22]. Secondly, the field is propagated to the exit plane of the CRL by a single FrFT transform. Thirdly, the field is multiplied by an effective pupil function (see Fig. 3(b)), which in combination with the vignetting function in the sample plane takes the attenuation of the CRL into account. In this step, as an option described below, the field is also multiplied by the cumulative phase errors of the CRL (see Fig. 3(c)). Finally, the field is propagated to the detector plane by a second FrFT transform, where the intensity pattern is calculated.

Phase errors are expected from CRLs [24], and are therefore included above. For these simulations we constructed an *ad hoc* phase distortion model by a radially symmetric cosine function with amplitude of 2π and a period of 0.5 mm. This model is qualitatively similar to [24], and represents the cumulative phase errors for the entire CRL.

Optics EXPRESS

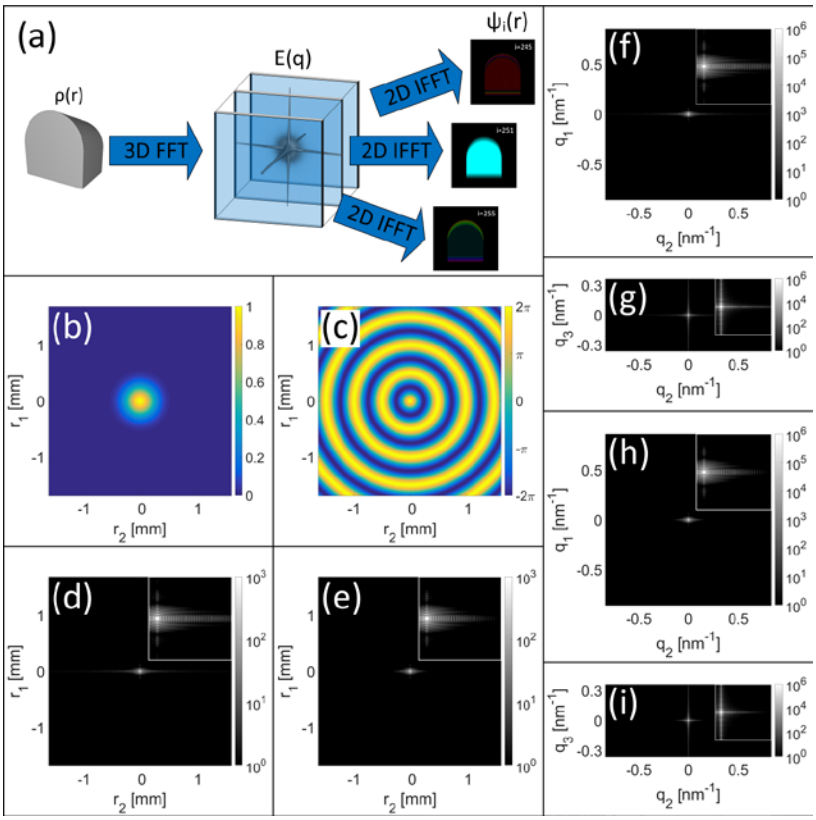

Fig. 3. Calculation of the 3D intensity patterns. (a) Calculation of the series of 2D exit-fields, $\psi_i(\mathbf{r})$, produced along the rocking curve through a single 3D forward Fourier transform (3D FFT) followed by a series of 2D inverse Fourier transforms (2D IFFT) of slices of the reciprocal space. The effective pupil function amplitude (b) and phase (c), in the ($\mathbf{r}_1$, $\mathbf{r}_2$) plane. (d) Amplitude of the exit field at the exit plane of the CRL without attenuation and (e) after applying the pupil function in (b)-(c), plotted on a logarithmic scale. (f)-(g) 2D intensity patterns in the detection frame along the ($\mathbf{q}_2$, $\mathbf{q}_1$) and ($\mathbf{q}_2$, $\mathbf{q}_3$) planes, respectively, for the BCDI case. (h)-(i) Same as (f)-(g), for the objective BCDI case. In (f)-(i), the intensity has been corrupted by Poisson shot noise, for a maximum of intensity of 1,000,000 counts; the intensity scale is logarithmic, and covers 6 orders of magnitude. The insets in (d)-(i) correspond to close-ups on the interference fringe distribution, which do not exhibit discernable differences.

3.4 Numerical parameters

For the numerical simulation, the following parameters are used: the beam energy is set to 17 keV (λ = 0.73 Å). The sample is pure Pt; using the (111) reflection the Bragg angle is θ_B = 9.26°. A 2D detector with 1030 × 1065 pixels of size 75 × 75 µm^2 is chosen (corresponding to the Dectris Eiger 1M detector), and for the lensless BCDI simulation it is placed at 4.0 m from the sample. In the rocking curve direction, performed in the vicinity of the $\mathbf{G}_{111}$ Bragg vector, we use an angular step size of $\delta\theta$ = 0.003°, and a total of 500 steps along the rocking curve resulting in a 3D data set of 1030 × 1065 × 500 voxels. With these settings the diffraction pattern is oversampled by a factor of approximately 4 in all directions. These parameters have been chosen to match an experimentally realizable setup.

For the objective BCDI setup we choose a Be CRL with N = 52 identical lenses spaced by T = 1.6 mm and an apex radius of curvature of R = 50 µm. This means that the focal length of one individual lenslet is f = 21.2 m, while the effective focal length of the entire CRL is f_N = 38.0 cm [20]. With a sample-lens distance of d_1 = 10 cm the Gaussian vignetting function has an RMS width of σ_v = 174 µm and the Gaussian angular acceptance function an RMS width of

Optics EXPRESS

σ_a = 782 µrad [20,22]. With this setup a virtual image is produced at d_2 = –25.7 cm, magnified by a factor of M = 1.5. To preserve the sampling ratio with respect to the no-lens case, the image-detector distance is set to 6.0 m, obtained by multiplying the standard sample-detector distance by the magnification. The image is behind the object, so the total object-detector distance in this case is 5.96 m. Using these parameters, and assuming a random texture, we estimate a probability of 0.15 of finding a grain in the diffraction condition within the probing volume. (This probability is calculated by considering the angular acceptance and vignetting width of the objective lens, giving the fraction of reciprocal space and real space being probed, respectively). Being well below 1, there is a good chance of imaging a single grain without overlap from neighboring grains.

3.5 Propagation results

Results of the successive steps of the calculation are shown in Fig. 3. The 2D wave-fields, obtained in the ($\mathbf{r}_1$, $\mathbf{r}_2$) plane taken at the exit of the CRL, are shown before and after the application of the pupil function, in (d) and (e), respectively. One can see that at this propagation distance, the Fresnel fringes are already well developed, implying that the propagation is not in the near-field regime anymore. Furthermore, the effect of the CRL is clearly evidenced as a cut-off of the high-angle fringes. Except for this cut-off the overall shape of the amplitude is very well preserved after the CRL. Next, in Figs. 3(f)-3(i), 2D intensity patterns for the lensless and the objective cases are compared along two cross-sections of the detection frame. As expected, the cut-off produced by the lens is only visible in the ($\mathbf{q}_1$, $\mathbf{q}_2$) plane, while the lens does not affect the intensity distribution along the $\mathbf{q}_3$ direction. Moreover, below the cut-off, the intensity distribution is very similar for the two configurations (3D renderings of the diffraction pattern without and with the objective lens are available as Visualization 2 and Visualization 3, respectively). These forward propagation results already indicate that the lens should only limit the resolution in the ($\mathbf{x}$,$\mathbf{y}$) plane of the object and that it should produce very little artifacts, as the intensity pattern is preserved below the cut-off. This will be further investigated in the next section.

4. Reconstructions of the 3D images

Identical reconstruction procedures were performed for the lensless BCDI and the objective BCDI configurations, using the simulated 3D intensity distributions described in the previous section. To discriminate between reconstruction artifacts related to the introduction of the objective lens and the photonic shot noise, two data sets were generated for each configuration, corresponding to different signal-to-noise ratios (SNR). For the high SNR case, the maximum intensity of the Bragg peak was set to 1,000,000 counts and the full 3D intensity pattern was corrupted by Poisson statistic fluctuations to account for the photonic shot noise. The lower SNR case was obtained by setting the intensity maximum to 50,000 counts before noise corruption. This latter intensity value corresponds to typical values extracted from the literature [6,25,26]. The effects of the shot noise on the diffraction pattern can be seen in Fig. 7, showing the ($\mathbf{q}_2$, $\mathbf{q}_1$)-plane both with and without the objective lens.

For both configurations the 3D image of the object was recovered by an iterative reconstruction using no *a priori* knowledge. The reconstruction involved applying two inversion algorithms alternately: the error reduction (ER) [27] and the hybrid input output (HIO) algorithms [28]. These inversion procedures are based on far-field regime propagation (Fraunhofer approximation) between the sample space and the detection space, so that a normal FFT operation can be used to account for the propagation of the field between the sample and the detection. In the 3D case, the FFT is directly applied to the 3D sample scattering function $\rho(\mathbf{r})$, in order to estimate the 3D "field distribution" in the vicinity of the Bragg peak. In each space, constraints are applied to enforce the solution to fulfill the intensity information measurement and the finite support condition simultaneously. Therefore a reasonable estimate

Optics EXPRESS

of the support function is initially needed. It is further refined during the inversion process by the application of the shrinkwrap algorithm [29].

For both high and low SNR and for both the lensless BCDI and the objective BCDI case we used identical parameters for all the reconstruction procedures. In practice, the rather large size of the individual data sets (1064 × 1030 × 500 points) leads to a time-consuming reconstruction process. To optimize the computing time, the data set was initially cropped to a smaller size (256 × 256 × 256 points), giving a corresponding low resolution object (and support). This initial reconstruction was done by running 10 HIO + 10 ER + 1 shrinkwrap steps for 69 cycles, and using $\beta = 0.9$ for the HIO steps [28]. The parameters for the shrinkwrap algorithm were: tolerance = 0.25, $\sigma_{\text{init}} = 2.0$, and $\sigma_{\text{end}} = 1.0$ [29]. This small data size allowed us to run the inversion on a GPU, so that it took only a few minutes to complete. In a second step, the retrieved wave-field was scaled up to the original size, leading to a decrease of the object (and support) voxel size. Then, 50 more cycles of 10 HIO + 10 ER + 1 shrinkwrap steps were run (with shrinkwrap parameters set to: tolerance = 0.15, $\sigma_{\text{init}} = 3.0$, and $\sigma_{\text{end}} = 1.8$), followed by 50 cycles of 10 HIO + 10 ER steps. During the last 1000 iterations, the object was averaged after each ER block (every 20 iterations) following the procedure in [30].

For the four cases above, the results of the reconstructions are shown along two orthogonal planes (**x**, **y**) and (**z**, **y**) in Fig. 4, while the differences between the retrieved objects and the original one (in amplitude and phase) are shown in Fig. 5, in the (**z**, **y**) plane. Figures 4(a) and 4(b) represent the reconstruction from the conventional BCDI setup with a high SNR (1,000,000 counts). This represents the figure of merit in the optimum case. The object is retrieved with minor artifacts across the sample, seen as small amplitude and phase fluctuations with high spatial frequency, clearly evidenced in Figs. 5(a) and 5(b), for amplitude and phase respectively. This high spatial frequency fluctuations results from the SNR value which produces intensity uncertainties at large wave-vector transfer. A similar representation is shown in Figs. 4(c) and 4(d) for the low SNR case (50,000 counts). As expected this reconstruction shows artifacts at a lower spatial frequency than the high SNR case (see also Figs. 5(c) and 5(d)). Interestingly, the straight edge perpendicular to the **x** axis is sharper, but we ascribe this observation to support effects: the support, which is retrieved along with the inversion procedure, was found to be 2 voxels narrower in the low SNR case (Figs. 4(c) and (d)). This leads to an artificially sharp interface along the **x** axis. The reconstructions obtained from data obtained with objective BCDI are shown in Figs. 4(e) and 4(f) for the high SNR case and in Figs. 4(g) and 4(h) for the low SNR case. The reconstruction quality is overall similar to the lensless case, with however some interesting effects: for the high SNR case, the phase and amplitude look smoother than the optimum case. This is a result of the cut-off induced by the lens aperture, which acts as a smoothing function in the sample space. A closer look at the phase and amplitude variations (Figs. 5(e) and 5(f)) shows the presence of very weak amplitude and phase fluctuations with low spatial frequency along the y-direction (the lens cut-off direction) and higher frequency along the z direction (the direction where only the SNR is the limiting factor). A corresponding decrease in resolution can be observed at the edge of the object, along the **x** and **y** directions, which look blurred with respect to the lensless BCDI case (Figs. 4(a) and 4(b)). Finally, the low SNR case shown in Figs. 4(g) and 4(h) exhibits larger amplitude and phase fluctuations, resulting from the noise effects acting at low spatial frequency, as seen in Figs. 5(g) and 5(h). Consequently, the resolution is degraded and results in an additional blurring of the object edges with respect to the high SNR objective BCDI case.

The resolution of the reconstructions has been investigated, assuming a Gaussian point spread function (PSF) and contrast limit of 26% (similar to the Rayleigh criterion). In the lensless case the resolution is 2-3 pixels in each direction, equivalent to 6-9 nm in the (**x**, **y**)-plane and 16-24 nm in **z**-direction. In the objective case the (**x**, **y**)-plane resolution is about 16 nm and 19 nm in the high SNR and low SNR simulations, respectively. In the **z**-direction the resolution is still 2-3 pixels, i.e. 16-24 nm.

Optics EXPRESS

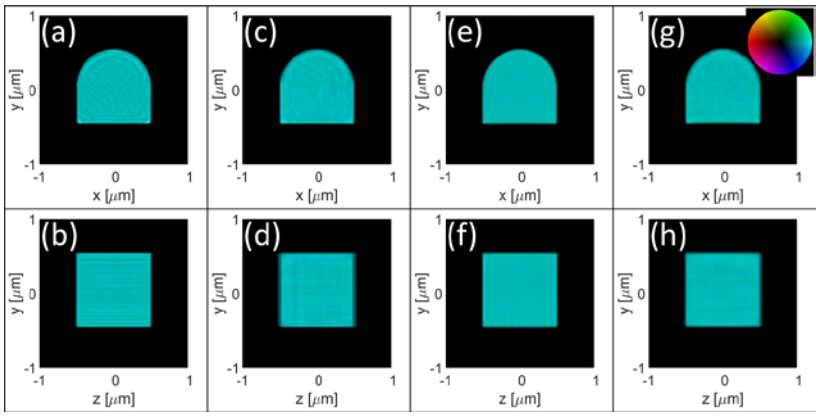

Fig. 4. 3D Reconstruction of the sample image. (a)-(b) Results of the reconstruction obtained for the lensless BCDI configuration with the high SNR data, shown in the (**x**, **y**) and (**z**, **y**) planes, respectively. (c)-(d) Same as (a)-(b), but for the low SNR data set. (e)-(f) Same as (a)-(b) but for the objective BCDI configuration. (g)-(h) Same as (e)-(f) but for the low SNR data set. The brightness encodes the amplitude and the color encodes the phase, as indicated by the color scale inset in (g) and is the same as in Fig. 2.

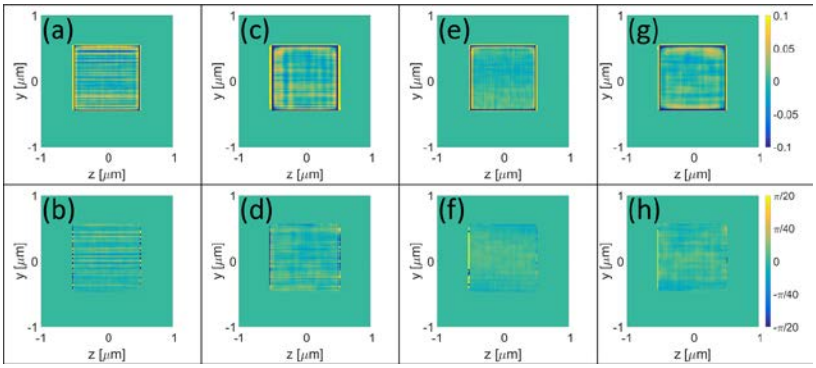

Fig. 5. Quality of (**z**, **y**) planes of the 3D reconstuctions shown in Fig. 4. Row above: amplitude difference between true object and retrived object with respect to color scale to the right of (g). Row below: phase difference between true object and retrived object with respect to color scale to the right of (h). (a)-(b) Lensless BCDI with high SNR. (c)-(d) Lensless BCDI with low SNR. (e)-(f) Objective BCDI with high SNR. (g)-(h) Objective BCDI with low SNR.

Overall, the quality of the retrieved images is very high, as demonstrated by the small amplitude and phase scales used for plotting the differences shown in Fig. 5. The fact that the phase of the retrieved object is only affected to a small degree by the introduction of a lens with a significant phase curvature and with aberrations may be surprising. To understand this, consider the calculations shown in Fig. 6. Figures 6(a) and 6(b) is the phase and amplitude of the object, respectively, as reconstructed by an inverse Fourier-transform of the complex-valued 3D diffracted-field obtained in the objective BCDI configuration. This object, highly distorted and containing severe phase variations, is evidently not a satisfying image of the original object, although it is the exact solution of the inverse problem. Figures 6(c) and 6(d) shows the result of the same calculation for a slightly different diffracted field, where its phase has been replaced by the phase of the diffracted field produced in the lensless BCDI case. The obtained object is of very high quality, almost indistinguishable from the original one. This means that the amplitude of the diffracted field in the objective BCDI configuration is only weakly affected by the phase shift introduced by the CRL, as this is positioned at a distance to the sample which is close to the far-field one. This also implies that the support information introduced in the iterative inversion algorithm is sufficient to retrieve the phase associated with

Optics EXPRESS

the free-space propagation. In other words, the fact that in BCDI the intensity is the only accessible information, together with the fact that this intensity is not affected by the phase shift introduced by the lens, allows preserving the information from the object. This effect can also be illustrated by comparing the complex-valued field produced by the lensless BCDI configuration (Fig. 6(e)), the field obtained after forward propagation through the CRL objective set-up (Fig. 6(f)) and the field retrieved from the reconstruction algorithm using the CRL objective set-up intensity information (Fig. 6(g)). As seen, Figs. 6(e) and 6(g) are almost indistinguishable.

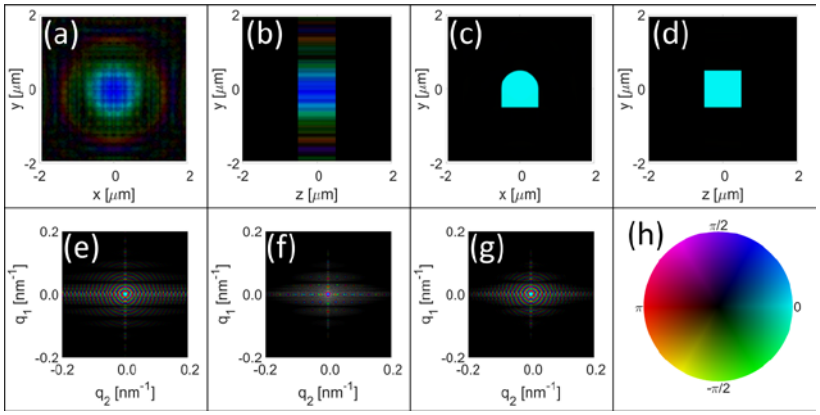

Fig. 6. Effect of the CRL objective phase aberrations. (a)-(b) The (**x**, **y**) and (**z**, **y**) planes of the direct inversion of the simulated diffracted field with the CRL. (c)-(d) Same as (a)-(b), but replacing the phase of the simulated diffracted field with the CRL by the phase obtained from the lensless propagation. (e) Amplitude and phase of the diffracted field in the lensless simulation. (f) Amplitude and phase of the diffracted field simulated using the CRL objective with aberrations. (g) Amplitude and phase of the reconstructed field from the intensity pattern obtained using the CRL objective with aberrations. (h) shows the colorscale used in all the plots, which is the same as in Figs. 2 and 4.

5. Discussion and conclusion

The above results clearly documents the potential of objective BCDI: the likelihood of superposition of the scattering patterns arising from simultaneously illuminated diffraction elements is reduced by orders of magnitude in the virtual image configuration used. The sampling of the diffraction pattern is identical to the lensless case, and the effect of aberrations on the diffraction patterns and the reconstruction quality is negligible because the introduction of the lens corresponds to a modification of the phase of the object far field pattern. The lens has a limited pupil size, which limits the maximum q-range that can be recorded in the ($\mathbf{q}_1$, $\mathbf{q}_2$)-plane and consequently the obtainable resolution in the (**x**, **y**)-plane of the object. However, in comparison to existing bulk mapping methods the resolution is still very favorable and the $\mathbf{q}_3$-direction is not impacted at all by the lens pupil.

In the following we discuss the quality of the reconstructions performed in more detail, address general limitations of the technique and comment on future applications.

5.1 Quality of reconstruction

The diffraction limit implies that the spatial resolution, as defined by the aperture of the lens, for our simulation is $r = 0.61\lambda / NA = 24$ nm. This is consistent with the resolution analysis on the reconstruction of the objective BCDI simulation. We speculate that better resolutions may be attainable with an improved numerical aperture.

The phase sensitivity, which can be evaluated by the amplitude of the phase fluctuations exhibited in our reconstructions, corresponds to a displacement on the order of 5 pm. This agrees with the usual performances of classical BCDI [31].

Optics EXPRESS

The new approach introduces new degrees of freedom such as magnification and sample-lens distance. In the example we chose $M = 1.5$ for the virtual image and $d_1 = 10$ cm, which are considered realistic parameters. An optimization of these with respect to time and space resolution, field-of-view, error-robustness and contrast will be sample specific as well as specific to the geometry of the laboratory and the lenses available and is outside the scope of this presentation.

5.2 Limitations of the method

- The photon statistics is quite favorable in the two simulated cases. Interestingly, reducing the number of photons will only serve to decrease the difference between the lensless and objective cases, as the photon statistics will become the dominant source of errors. In practice, we expect the number of photons to be strongly dependent on the efficiency of the lens. Notably, the increase in coherence flux, which is expected with new or upgraded synchrotron sources may compensate for this loss.

- In the simulations shown, we only presented a strain-free object in order to identify resolution and sensitivity issues. As the reconstruction principle is the same with and without the lens we do not anticipate restrictions for including strain beyond those applying to existing BCDI algorithms today. We performed preliminary tests that showed equal reconstruction quality for strained objects. More sophisticated BCDI algorithms taking into account e.g. partial coherence may also be generalized to the objective BCDI.

- The optical properties of the objective, including aberrations, will naturally be a limitation. Studies of bulk materials require hard X-rays, and so far the choice of optics for full field microscopy has been compound refractive lenses, CRLs [19,32–34]. These have tunable vignetting widths as the number of lenses can be varied, and it is possible to calculate their optical performance analytically [20]. But the pupil function width is inversely proportional to the vignetting width, and the focal length of the lens is affected by the number of lenses as well. Hence a compromise between these three parameters must be made. This optimization procedure is subject to various experimental constraints and is beyond the scope of this article. Another problem is manufacturing errors. Given the *ad hoc* description of the phase errors, the reconstructions were surprisingly tolerant of this. More work is required to determine whether this result reflects actual performance. Alternatively, one might introduce other lens technologies, such as multi-layer Laue lenses (MLLs). For these lenses the acceptance angle is more complicated, but around 2 mrad (FWHM) has been demonstrated in [35]. In the case of a wedged MLL the focal length and aperture may be chosen freely in principle, but in this case the physical aperture is limited [36,37].

- Despite the reduction in sampling the volume, hundreds of grains may still be within the volume, thus putting restrictions on the types of samples that can be measured. E.g. highly textured samples may be impossible to characterize, as most grains will have nearly identical orientations. In these simulations the probing volume is limited by the intrinsic vignetting width of the objective lens. However, further reduction in the probing volume may be achieved by inserting a slit in the image plane when using a real image geometry.

5.3 Further perspectives

We left out simulations using a real image configuration. However, we foresee that it might be interesting to investigate reconstructions based on simultaneous measurements in the image plane and far field diffraction plane, specifically for samples presenting non-homogenous strain fields. Indeed this combined information arising from two conjugated spaces should lead to an

Optics EXPRESS

improvement of the BCDI robustness with respect to strain field imaging. This will require an optimized reconstruction algorithm.

For crystals larger than the beam coherence length, or whose sizes do not fulfill the oversampling conditions, the presented modality can be combined with a ptychography approach [38]. We expect that the Bragg ptychography reconstruction will be eased by the combined knowledge of the finite incident beam size and finite exit direction, allowing to restrict the scattering volume in 3D [39] and eventually opening the possibility to scan the sample along the three space directions. This new modality will be investigated in the near future. It could provide a solution to the imaging of textured samples.

Experimental demonstrations are under development. Notably, objective BCDI can be implemented at existing synchrotron setups. One option is to use a beamline optimized for classical BCDI and add the objective. Another option is to use an existing DFXRM beamline and collimate the incoming beam sufficiently to make a coherent volume fraction matching the requirements of classical BCDI.

Appendix

Additional diffraction pattern images

Figure 7 shows the influence of noise on the diffraction pattern, as discussed in section 4 above.

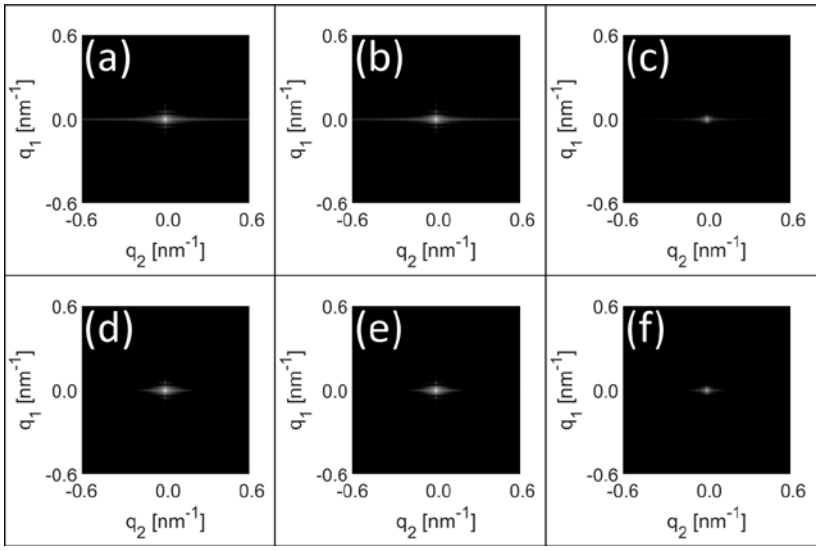

Fig. 7. The ($\mathbf{q}_2$, $\mathbf{q}_1$)-plane of the 3D diffraction pattern is shown using a conventional BCDI setup (a)-(c), and with an objective lens (d)-(f). In both cases the images have either no noise (a) and (d), 1,000,000 photons in the brightest pixel (b) and (e), or 50,000 photons in the brightest pixel (c) and (f). In all cases the intensity is shown on a logarithmic scale and shows the same 6 orders of magnitude.

Funding

European Research Council (ERC) Advanced Grant (291321-D-TXM); DanMAX (4059-00009B).

Acknowledgment

The authors would like to thank M. Allain for fruitful discussions.